High aspect ratio induced spontaneous generation of monodisperse picolitre droplets for digital PCR

Xiaonan Xu,[1] Haojun Yuan,[2] Ruyuan Song,[3] Miao Yu,[1] Ho Yin Chung,[1] Youmin Hou,[1] Yuhe Shang,[1] Hongbo Zhou,[2] and Shuhuai Yao[1,3,a)]

[1]*Department of Mechanical and Aerospace Engineering, The Hong Kong University of Science and Technology, Hong Kong, China*
[2]*State Key Laboratory of Transducer Technology, Shanghai Institute of Microsystem and Information Technology, Chinese Academy of Science, Shanghai, China*
[3]*Department of Chemical and Biological Engineering, The Hong Kong University of Science and Technology, Hong Kong, China*

Droplet microfluidics, which involves micrometer-sized emulsion droplets on a microfabricated platform, has been demonstrated as a unique system for many biological and chemical applications. Robust and scalable generation of monodisperse droplets at high throughput is of fundamental importance for droplet microfluidics. Classic designs for droplet generation employ shear fluid dynamics to induce the breakup of droplets in a two-phase flow and the droplet size is sensitive to flow rate fluctuations, often resulting in polydispersity. In this paper, we show spontaneous emulsification by a high aspect ratio (>3.5) rectangular nozzle structure. Due to the confinement and abrupt change of the structure, a Laplace pressure difference is generated between the dispersed and continuous phases, and causes the thread thinning and droplet pinch-off without the need to precisely control external flow conditions. A high-throughput droplet generator was developed by parallelization of a massive number of the basic structures. This device enabled facile and rapid partition of aqueous samples into millions of uniform picolitre droplets in oil. Using this device, on-chip droplet-based digital polymerase chain reaction (PCR) was performed for absolute quantification of rare genes with a wide dynamic range. *Published by AIP Publishing.* https://doi.org/10.1063/1.5011240

I. INTRODUCTION

Droplets or emulsions in microfluidic systems can work as "miniaturized mobile reactors" for chemical and biological assays,[1–3] owing to their unique features such as high-throughput, rapid response, being contamination-free, requiring minimal reagent volume, and isolation of individual space. For instance, the commercialized droplet-based digital polymerase chain reaction (PCR) technology,[4–7] in which a diluted sample is partitioned into a sufficient number of reaction aliquots that allow single-molecule amplification and absolute quantification of the target gene, has attracted tremendous interest in various applications, from prenatal screening of fetal genomic abnormalities and inherited disorders to rare sequence detection of cancer and infectious diseases.[8–13] In the food, pharmaceutical, cosmetic and oil industries, monodisperse emulsions with well-defined compositions are highly desired and widely used as templates for microparticle or microcapsule fabrication.[14–19]

In microfluidic systems, the dynamics of droplet formation is dominated by the balance of tangential shear stresses and interfacial tension.[20,21] In shear-based systems that usually include T-junction, flow-focusing, or co-flow designs, the hydrodynamic force is employed for breaking the stream into droplets by the coupling of the two-phase flow rates, fluid properties, and nozzle

---

a)Author to whom correspondence should be addressed: meshyao@ust.hk

geometry. Tight control over the flow conditions of the dispersed and continuous phases is demanded for generating monodisperse droplets.[22] Variation in one of the parameters would result in different trains of droplets, which makes large-scale parallelization of basic units for scalable production difficult.[23] Recently, Teo *et al.*[24] demonstrated negative pressure controlled droplet generation in a flow-focusing device. Although large-scale integration can be made feasible by one negative pressure source through careful design of fluidic flow networks, the pressure sensitive issue still cannot be circumvented. Instead, in interfacial tension driven systems, e.g., step emulsification,[25] the abrupt height change induces a Laplace pressure difference for spontaneous droplet generation, which is insensitive to the flow rate or pressure. The droplet self-breakup process is predominantly driven by the interface between the two phases, thus eliminating the shear stress interference. To date, various self-emulsification structures have been developed including the grooved-type microchannel,[26] straight-through microchannel,[27–29] edge-based droplet generation (EDGE),[30] and gradient of confinement.[31] Droplet production scale-up is possible by massive parallelization of these basic structures. For instance, Kobayashi *et al.*,[27,32,33] Dangla *et al.*,[31] and Amstad *et al.*[23,34] parallelized the step emulsion arrays for droplet massive production. Nevertheless, the development of interfacial tension induced droplet generators has been hindered for widespread adoption due to less robustness in device operation or the cumbersome process for device fabrication.

    In this paper, we present a simple yet efficient structure for droplet spontaneous generation. It is found that in a rectangular microchannel, usually with an aspect ratio larger than 3.5, the dispersed phase fluid thread is able to self-breakup into monodisperse droplets when entering the chamber filled with fluid of continuous phase as shown in Fig. 1. The interface of the two phases is initially confined in an energy unfavorable shape by the narrow channel till it arrives at the nozzle with an opening junction where the strong confinement is released in the horizontal direction. Due to this abrupt change, the equilibrium status of the Laplace pressure cannot be maintained, which triggers the interface thread necking and droplet formation. Such an intrinsic droplet breakup mechanism decouples the shear stress interference and thus is independent of fluid properties and flow rates. The resulting droplet size is solely determined by the width of the nozzle and not sensitive to flow fluctuations. Comparing with the above mentioned interfacial tension driven self-emulsification structures,[25–30] this high aspect ratio induced droplet self-breakup (HIDS) structure has a very simple geometry and is easy to fabricate. It is possible to parallelize the HIDS structures in a more compact configuration for high throughput droplet production. Hence, we developed a fishbone droplet generator by parallelizing 2000 HIDS units to produce monodisperse picolitre droplets with coefficients of variation below 3% at a generation rate of 15 kHz. By using the HIDS based droplet generation device, we demonstrated an on-chip droplet-based digital PCR system which involved the sample partition, *in situ* thermal amplification, and end-point fluorescence readout in one chip, exhibiting the capability for highly sensitive and efficient detection of targeted DNA fragments in extremely low abundance.
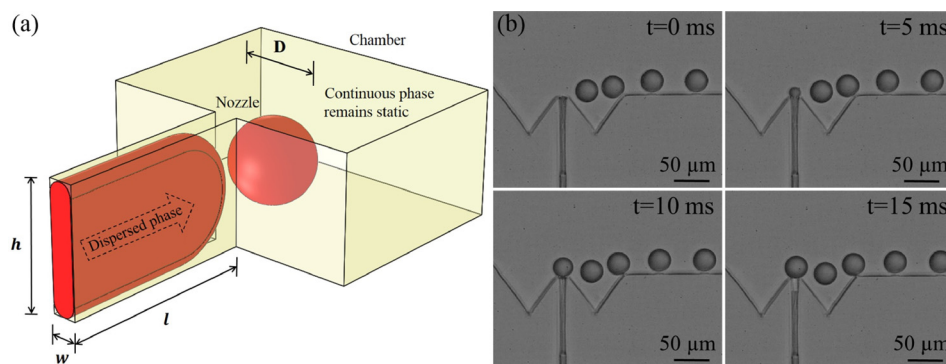

FIG. 1. (a) Schematic showing the high aspect ratio induced self-breakup (HIDS) structure for droplet generation; (b) time-lapse images showing the droplet generation in HIDS.

II. MATERIALS AND METHODS

A. Device fabrication

The microfluidic device was made of polydimethylsiloxane (PDMS) (Sylgard 184 silicone elastomer, Dow Corning) using a micromolding process.[35,36] The microchannels were patterned on a silicon wafer by photolithographic patterning (SUSS Microtec MA6) and etched by deep reactive ion etching (STS ICP DRIE Silicon Etcher) to serve as a mold for PDMS replica molding. The silicon mold was then put in a vacuum chamber with a few drops of trichloro(1H,1H,2H,2H-perfluorooctyl)silane (Sigma-Aldrich) to prevent the PDMS from sticking to the mold. A PDMS mixture (in a 10:1 ratio of monomer and curing agent) was cast on top of the silicon mold, degassed in vacuum and cured in a 70 °C oven for 2 h. Afterwards, the cured PDMS was released from the silicon mold and cut into individual chips. The access holes for the liquid inlet and outlet were punched using a pan needle. The PDMS replica and a glass slide (SAIL BRAND, China) were treated with O_2 plasma and bonded together. For generating water-in-oil droplets, the devices were baked on a hot plate at 100 °C for 8 h to recover the surface hydrophobicity. For oil-in-water emulsification, the device was simply filled with water after plasma bonding to maintain the hydrophilic surface.[37,38]

B. Preparation of PCR reagents

The DNA templates used here were the genomic DNA (gDNA) purified from lung cancer cell lines H1579 using a QIAprep Blood and Cell Culture DNA Medi Kit (Qiagen) according to the manufacturer's protocol. The DNA concentration was calibrated using Quant-iT PicoGreen dsDNA Kits (Invitrogen). The calibrated solution was then diluted into a series of sample solutions with a copy number of 10^1 to 10^6 copies/μl. All DNA samples were stored at -20 °C prior to use. The primers and probes were designed with the Primer premier 5 software according to the EGFR gDNA sequence. A pair of primers (Forward primer: 5′-TTCCCATGATGATCTGTCCCTC-3′. Reverse primer: 5′-CACCTCCTTACTTTGCCT-3′) was used to amplify a 214 bp product of EGFR exon 21 sequence. A HEX dye-labelled MGB hydrolysis probe (5′ HEX-CCAAGCGACGGTCCTC-MGB 3′, Invitrogen) was used to trace all the PCR products. The PCR mixture in a total volume of 20 μl contained 5 μl of 2× Light Cycler 480 Probe Master, 0.2U of Uracil DNA Glycosylase (Takara, Japan), 400 nM each of forward and reverse primers, 250 nM MGB probe, and the gDNA sample of various concentrations. All reaction components, including the PCR master mix, primers, probes, and DNA template, were premixed off-chip before sampling.

C. Device operation and droplet-based digital PCR assay

To generate water droplets using a HIDS device, mineral oil (BioReagent for molecular biology, Sigma-Aldrich, viscosity: 14.2 cSt) with surfactants as the continuous phase was first filled with in the device channels to eliminate all the air bubbles in the device. The dispersed phase (water) was then pressurized by a syringe pump from the inlet to pass through the channel network. To examine the droplet formation mechanism and size dependence, the flow rates of the dispersed and continuous phases were, respectively, varied by precise syringe pumps with ±0.25% accuracy (PHD ULTRA, Harvard Apparatus). The interfacial tension of the water-mineral oil containing 3 wt. % Abil EM 90 was measured as 4.7 mN/m.

In droplet-based digital PCR assay, the PCR mixture was partitioned into droplets using an integrated HIDS droplet generator. The continuous phase was mineral oil combined with the stabilizing surfactants 3 wt. % ABIL EM 90 and 0.1 wt. % Trixon X-100.[12,39,40] ABIL EM90 is a silicone-based surfactant which serves two purposes for emulsion PCR:[41] First, it prevents droplet coalescence in thermocycling. Second, it reduces DNA polymerase adsorption on the water-oil interface which would affect the PCR efficiency. Triton-100 is a non-ionic addictive used to suppress secondary structure formation and help stabilize the DNA polymerase.[42] The interfacial tension of the PCR mixture with mineral oil and surfactants 3 wt. % ABIL EM 90 and 0.1 wt. % Trixon X-100 was 2.5 mN/m. PCR sample evaporation is a serious issue in

PDMS devices during the heating and cooling process as PDMS is highly permeable.[43–46] To tackle this issue, we made a droplet storage chamber which comprised of two $1'' \times 3''$ glass slides (SAIL BRAND, China) with spacers of the desired depth and sealed with epoxy (Araldite, Huntsman Advanced Materials) on the corners. In this work, since the designed droplet diameter was $18\,\mu m$, we used foil paper with a thickness of $20\,\mu m$ for the spacers to make sure that the produced droplets spread in one layer in the glass chamber. The droplets were then sucked into the glass chamber due to the capillary effect. The edges of the glass chamber were sealed with epoxy after the completion of sample partitioning to prevent the oil and water evaporation. The device was placed on a flat thermal cycler (Mastercycler Nexus, Eppendorf) to conduct the thermocycling. For the thermal amplification, the temperature setting was 5–10 min of preheating at 95 °C for double-stranded DNA melting or denaturation followed by 95 °C for 10 s and 60 °C for 30 s and repeated for 35 cycles. Once the reaction finished, the device was transferred to an inverted epifluorescence microscope (Eclipse Ti-U, Nikon) with an automatic XY motorized stage to capture the images of the whole droplet storage chamber. The fluorescent droplets were illuminated by a fiber illuminator (Nikon Intensilight C-HGFI) at an intensity of 50 mW through a filter cube for HEX dye, and recorded by a CCD camera (EXi Blue, QImaging). The images were analyzed using a custom-made image analysis software based on MATLAB.

III. RESULTS AND DISCUSSION

A. Simulation and experimental characterization of droplet formation

Figure 1(a) schematically shows the water-oil interface in a high aspect ratio rectangular nozzle which opens up to a chamber of the same height. The chamber is initially prefilled with oil as the continuous phase. Water as the dispersed phase is then pressurized into the high aspect ratio channel. Figure 1(b) shows the droplet generation process recorded by a high-speed camera. Monodisperse droplets are formed periodically at the exit of the nozzle. The water-oil interface forms a thin thread and pinches off into a droplet by Plateau–Rayleigh instability. Once a droplet leaves the nozzle, the elongated thread retracts and resumes the initial state.

To investigate the high aspect ratio induced droplet self-breakup mechanism, we carried out the computational fluid dynamics (CFD) simulations for the two-phase flow using a commercial software package ANSYS Fluent. Volume of the fluid model was employed to track the volume fraction of the dispersed and continuous phases (i.e., water and oil, respectively) to capture the droplet breakup process. In the simulation, we kept the width of the channel $w = 5\,\mu m$ while changed the height of the channel h from $10\,\mu m$ to $45\,\mu m$. The velocity from the inlet was set as $V = 0.002\,\text{m/s}$. The capillary number of the dispersed phase ($Ca = \mu V/\gamma$, where μ and V are the dynamic viscosity and velocity of the dispersed phase, and γ is the interfacial tension of the two phase system) was $Ca = 6.7 \times 10^{-4}$. Figure 2 shows the simulation results showing the snapshots during the interface deformation and droplet formation for typical cases. At low aspect ratios [$h/w = 2$–3, e.g., Fig. 2(a)], the interface gradually forms into a large pancake shape confined by the chamber wall. In contrast, at high aspect ratios [$h/w = 4$–9, e.g., Figs. 2(b) and 2(c)], as the interface elongates and grows into a spherical shape, the confined thread is triggered for necking in the vertical direction and pinches off into a droplet. In analyzing the velocity fields, we found that the difference between the cases of high and low aspect ratios is the backflow of the continuous phase fluid. The continuous phase flows back into the high aspect ratio nozzle so that it facilitates the thread thinning and droplet pinch-off. Because the thread necking occurs in the vertical direction, this process cannot be easily observed under the microscope. The simulation results provide a good basis to further understand the interfacial tension driven droplet breakup process.

We applied the Laplace pressure jump theory to analyze the droplet breakup process.[31,47–51] Figure 3 schematically shows the thread elongation and droplet breakup in a high aspect ratio channel. Here, the height is sufficiently large for the resulting droplet to maintain a spherical shape instead of being bounded by the upper and lower chamber walls to form a pancake. Provided that the injection flow rate is extremely low, the interface profile of the droplet
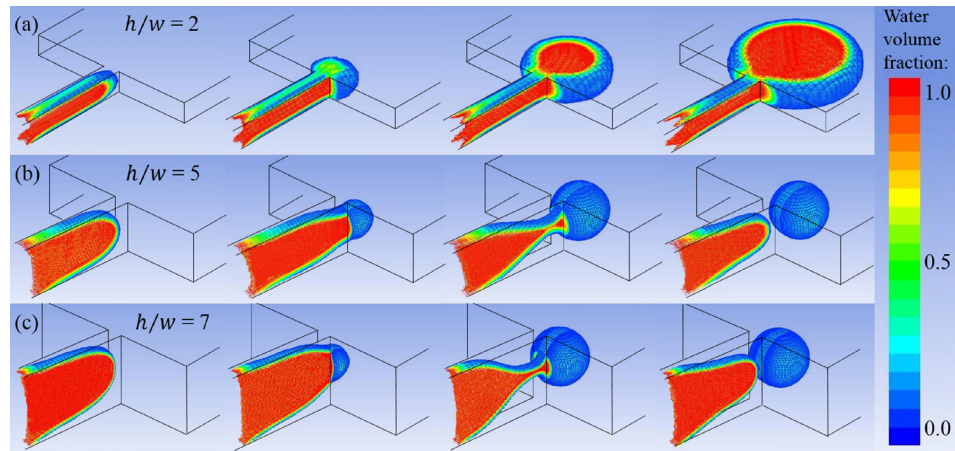
FIG. 2. CFD simulations of the droplet self-breakup in HIDS structures with w = 5 μm at different aspect ratios and: (a) h/w = 2, the thread grows into a pancake shape and the interface does not break up. (b) and (c) h/w = 5 and h/w = 7, the thread elongates confined by the narrow channel, and finally breaks into a droplet. Volume of the fluid model was used in the simulation. The volume fraction 1 represents the water phase, while 0 represents the oil phase.

breakup process evolves in a quasi-static situation. From the Young-Laplace equation: $P_i - P_o = \gamma(1/R_1 + 1/R_2)$ with R1 and R2 as the in-plane (in x-y plane) and transverse (in y-z plane) radii of the fluid interface, which relates the curvatures to the difference between the inner and outer pressures. As the inner and outer pressures are constant, in the quasi-static system, the curvature of the fluid interface must be equilibrated everywhere at every instant. Based on the CFD simulation results, the droplet breakup process can be divided into three stages as shown in Fig. 3. In stage I, as the interface proceeds in the high aspect channel, the interface is forced to follow the wall geometry in a compressed and energy unfavorable shape. The curvature of the thread confined in the high aspect ratio channel has a lower bound k^* ($k^* = 2/w$) which is determined by the width of the channel in the transverse plane.[48] In stage II, when the thread arrives at the junction, the strong confinement of the interface is released and starts to form a tongue in a spherical shape. According to the quasi-static hypothesis, the curvature of
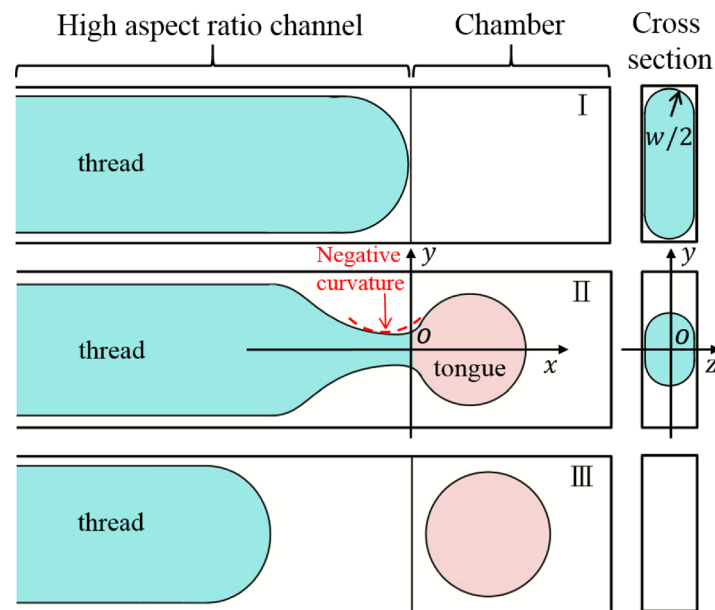

FIG. 3. Schematic of the thread elongation and droplet breakup in a high aspect ratio channel connecting to a chamber. The coordinate system (x, y, z) of the origin O at the centre of the nozzle as shown in both cross-sectional views.

the tongue should be equal to the curvature of the thread. As the tongue grows, the curvature of the tongue continuously decreases. When the radius of the tongue exceeds w, with the lower bound ($k^* = 2/w$) of transverse curvature of the thread, the in-plane curvature of the thread would take a negative value in an attempt to match the curvatures of the tongue. At this instant, the system comes out of equilibrium and starts the thread necking. In the HIDS nozzle where the thread takes a negative curvature, the local pressure drops abruptly, which leads to the backflow of the continuous phase of fluid to pinch off the thread into a droplet. After the droplet breaks up, the thread retracts back to the nozzle as shown in stage III in Fig. 3. The intrinsic droplet breakup mechanism indicates that the interfacial tension is the dominant force, which ensures the robustness to generate uniform droplets using the HIDS structure.

By further varying the aspect ratio h/w, we found a critical value of h/w = ∼3.5, below which the thread enlarges into a pancake shape and hardly breaks off. For h/w greater than 3.5, uniform droplets are formed continuously from the high aspect ratio nozzle, and the resulting droplet diameter is invariant with the height of the channel. To verify these results, we tested seven devices that have a channel width at $w = 5$ μm and the channel height varies at $h = 10, 15, 20, 25, 30, 35,$ and $40\,\mu$m, respectively. The capillary number of the dispersed phase was controlled within $Ca < 5 \times 10^{-4}$ which was consistent with the simulation condition. The experimental and simulation results are shown in Fig. 4(a). In the regime where h/w < 3.5, the droplet grows into a pancake shape and results in highly polydispersed droplet population. However, in the regime where h/w > 3.5, the fluid thread breaks up into uniform spherical droplets and the size remains almost the same as the height of the channel increases. Next, we studied the parameters of the channel geometry that determined the resulting droplet diameter. We characterized the droplet size produced by eight devices, in which the channel widths varied from 4 μm to 14 μm, and the aspect ratio was kept at 4. We plotted the measured droplet diameter as a function of the channel width and compared with the simulation results as shown in Fig. 4(b). We found that the droplet diameter (D) nearly linearly scales with the width of the channel, approximated as $D = 3.5w$, which also suggest that the droplet can grow in a spherical shape without boundary confinement when the height of the chamber is larger than 3.5w. Therefore, for a channel of aspect ratio (h/w) larger than 3.5, the fluid thread is able to self-break up into monodisperse droplets upon entering the chamber.

B. Parallelization for high throughput production

Enhancing droplet microfluidics throughput by parallelization is challenging in flow focusing and T-junction geometries. Because the droplet breakup is governed by the viscous shearing forces of the two phase flows, any pressure fluctuations in the integrated flow systems may lead to polydisperse droplet populations.[52–55]
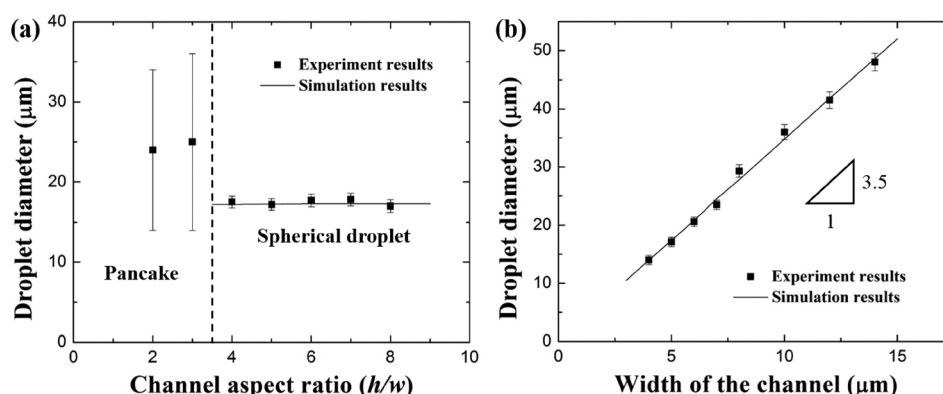

FIG. 4. Simulation and experimental results of the droplet size in different cases: (a) Droplet diameter variation as the increase of the aspect ratio of the HIDS channel (h/w). The width of the channel was kept at 5 μm. (b) Droplet diameter versus the width of the HIDS channel. The aspect ratio (**h/w**) was kept at 4. The slope of the curve was found to be 3.5.

The above droplet scaling analysis shows that the droplet size in the dripping regime in HIDS is governed only by the dimensions of the channel, given that the interfacial tension driven droplet breakup mechanism enables decoupling of the shear stress interferences. As there is no need to control the flow rates precisely, we can take advantage of this simple yet robust design for massive parallelization in an integrated device. We developed a "fishbone" device with thousands of HIDS units parallelized in line for droplet generation (Fig. 5). Only one pressure source was required to be applied to drive the dispersed phase fluid to pass through the HIDS network. The continuous phase fluid from the other inlet which can be driven by gravity or other external forces formed a crossing flow to sweep the produced droplets downstream for collection, making the droplet production continuous and stable.

Figure 5(b) shows the "fishbone" device that integrates 2000 HIDS structures of $7\,\mu m$ in width and $35\,\mu m$ in height, and generates highly uniform aqueous droplets of 6.4 pl in oil. The droplet generation frequency was $\sim 15\,kHz$ with a coefficient of variation smaller than 0.03. As shown in Fig. 5(c), within a specific range from 0.5 to $6.2\,\mu l/min$, the increase of the flow rate of the dispersed phase has a minimum effect on the resulting droplet size. Beyond the critical value ($\sim 6.2\,\mu l/min$), some of the in line arranging HIDS nozzles in the downstream position produced larger droplets in a pancake shape and resulted in polydisperse droplets. On the other hand, the flow rate of the crossing carrier oil phase has little influence on the produced droplet size as shown in Fig. 5(d). This is of significant importance for real applications where the fluid environment is much more complicated than in the experimental setting.[26,56] Also, precise fluid control pumps are not necessary for droplet generation, which could make the production system low-cost and reliable.

C. On-chip droplet-based digital PCR

We integrated the fishbone droplet generator with a glass chamber for on-chip droplet-based digital PCR as shown in Fig. 6(a). The setup included two components, the droplet
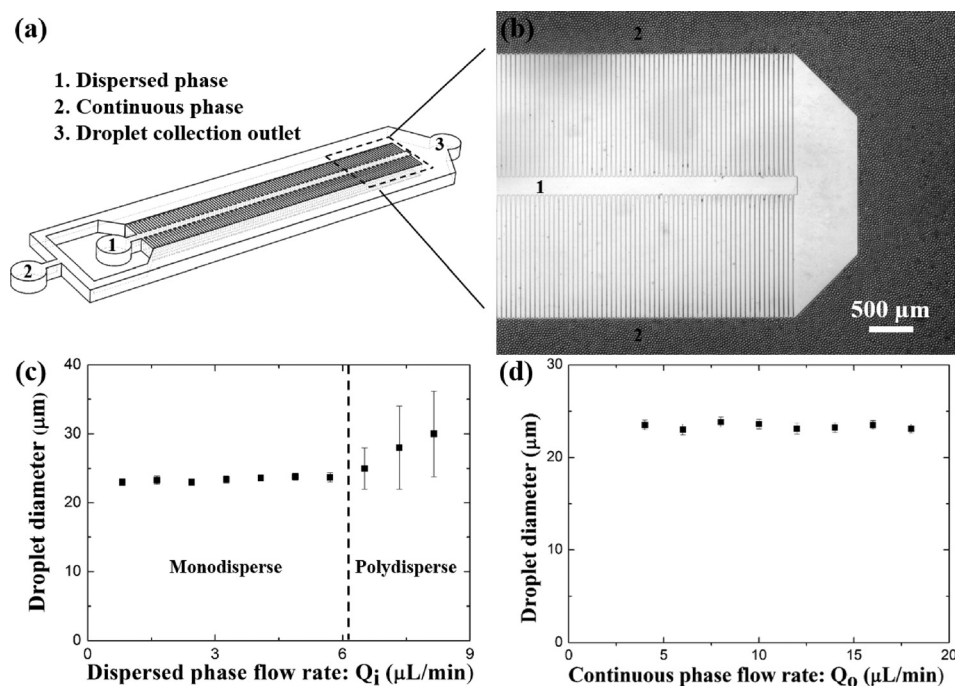

FIG. 5. (a) Schematic of the arrangement of the HIDS structures in a fishbone device. Inlet 1 is for the dispersed phase and inlet 2 is for the continuous phase. Produced droplets were swept by the crossing carrier oil and collected from the outlet 3. (b) Image of the fishbone device. Each HIDS channel is $7\,\mu m$ in width and $35\,\mu m$ in height, and the resulting droplet diameter is $23\,\mu m$. (c) and (d) Diameter of the produced droplets as variation of the flow rates of the dispersed and continuous phases. In (c), the flow rate of the disperse phase varied as the continuous phase was kept at $8\,\mu l/min$, while the flow rate of the continuous phase varied as the dispersed phase was kept at $3.2\,\mu l/min$ in (d).

generator, and droplet storage chamber. The glass sandwiched chamber here served two purposes, to prevent the droplet evaporation during the thermocycling and to confine the droplets in one layer for observation. In our experiments, the fishbone device was composed of 250 HIDS units for generating droplets of 18 μm in diameter (3 pl). Based on our calibration experiments (Fig. 5), we found that the continuous phase flow rate almost had no influence on the droplet size when it was kept very low, and only the dispersed phase flow rate range need to be controlled by the syringe pump. Here, the oil phase was driven by the gravity force by simply plugging a pipette tip at the oil inlet. A total volume of 20 μl PCR mixture containing DNA template, primers, master mix, and probes was pressurized to pass the HIDS network for droplet generation. The produced droplets were swept out from the edge of the device and were sucked into a 20 μm-high glass chamber by the capillary force. Due to the confinement in depth, the droplets spread out in a single layer in the glass chamber. The sample compartmentalization result is shown in the inset of Fig. 6(a). In 10 min, the PCR sample partition was accomplished and the device was placed on the thermal cycler for on-chip PCR amplification. According to the primer concentration, we calculated the average primer number encapsulated in one droplet to estimate the cycle number that was necessary for one DNA template to amplify in the exponential fashion (2^n) until saturated. In our experimental settings, 25 to 35 cycles were sufficient for the PCR amplification.

After the completion of thermocycling, we placed the device for end-point fluorescence readout under the microscope with a motorized platform. In fluorescent dye HEX (Ex: 535 nm, Em: 556 nm) and bright field microscopy, the whole droplet storage chamber was scanned and the images were taken automatically. After all the images were obtained, we used the customized Matlab programme to stitch the images and count the positive and negative droplet numbers. In each sample, one million droplets were counted for data analysis. By using the Poisson statics equation,[57] we calculated the absolute target DNA concentration. The entire experiment could be completed within ~40 min. Next, we performed calibration experiments with samples of certain concentrations (expected value) to determine the dynamic range and detection limit. Following the image analysis, we determined the corresponding DNA copy numbers (observed
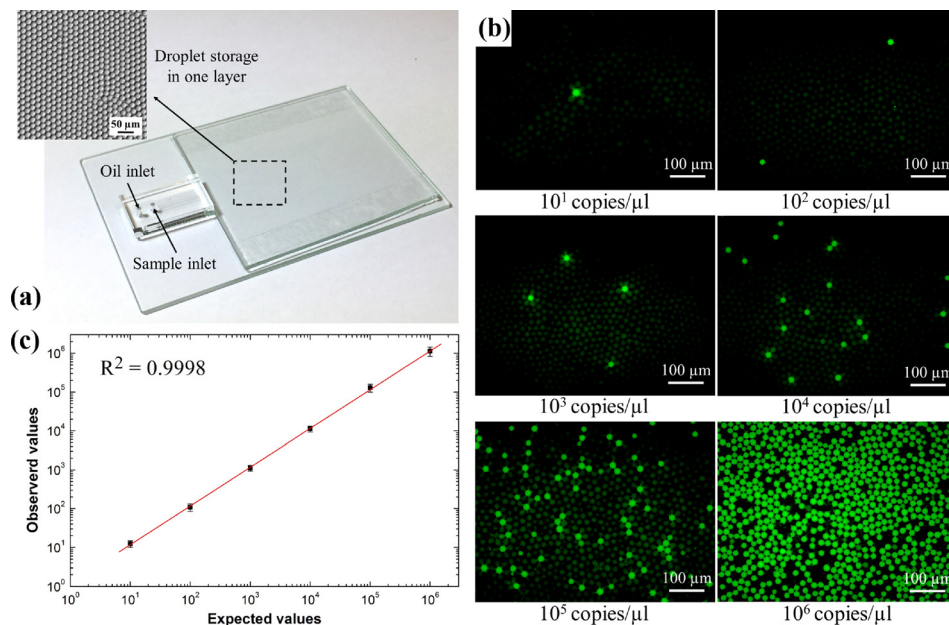

FIG. 6. (a) Image showing the setup for on-chip droplet-based digital PCR. The fishbone droplet generator device is integrated with a glass chamber for droplet storage. Inset: droplets spread in one layer in the glass chamber. (b) The observed values calculated from Poisson statistics by counting positive droplets match well with the expected values by performing a ten-fold serial dilution. (c) Fluorescent readout of the on-chip droplet-based digital PCR results which quantifies the target genomic DNA purified from lung cancer cell lines H1579 with a range of concentration from 10^1–10^6 copies/μl.

value) and plotted the calibration curve in Fig. 6(c). Figure 6(b) shows the fluorescence readout of different template concentrations ranging from 10^1 copies/μl to 10^6 copies/μl. To prove the robustness of the droplet-based digital PCR platform, each experiment with the sample of the same template concentration was repeated three times. The error bar in Fig. 6(c) shows that the results were consistent in different runs. The linearity between the observed value and expected value is 0.9998. Due to the picolitre droplet size and the million scale of the partition number, the detection limit can reach a few copies/μl and the dynamic range is allowed to reach almost 6 orders of magnitude. We have demonstrated that the integrated workflow of the on-chip droplet-based digital PCR can avoid the droplet loss, shorten the experimental hands-on time, and minimize the contamination during the transferring steps.[57,58] This integrated digital PCR system may serve as a powerful platform for rare gene detection and quantification.

IV. CONCLUSIONS

In this paper, we report that a high aspect ratio rectangular nozzle structure is able to induce the water-oil interface breakup for spontaneous droplet generation. From both CFD simulations and experimental characterization, we found that when the aspect ratio (h/w) was greater than 3.5, uniform droplets were formed and the resulting droplet diameter was invariant with the height of the channel. Within a certain flow range, the droplet size was insensitive to the flow fluctuations, which made the HIDS structure of great advantage for massive parallelization. We therefore developed a fishbone device by integrating 2000 HIDS units to produce uniform droplets that comprised the merits of ultrahigh throughput and operation robustness. This droplet generator has been demonstrated as a maneuverable and integrable device for on-chip droplet-based digital PCR for low abundance nucleic acid absolute quantification. We believe that this new design for high-throughput droplet generation will have a profound impact on the applications of droplet microfluidics for chemical and biological assays.

ACKNOWLEDGMENTS

[1] A. B. Theberge, F. Courtois, Y. Schaerli, M. Fischlechner, C. Abell, F. Hollfelder, and W. T. Huck, Angew. Chem., Int. Ed. **49**, 5846 (2010).
[2] P. Neuži, S. Giselbrecht, K. Länge, T. J. Huang, and A. Manz, Nat. Rev. Drug Discovery **11**, 620 (2012).
[3] K. S. Elvira, X. C. I. Solvas, and R. C. Wootton, Nat. Chem. **5**, 905 (2013).
[4] L. Dong, Y. Meng, Z. Sui, J. Wang, L. Wu, and B. Fu, Sci. Rep. **5**, 13174 (2015).
[5] F. Shen, W. Du, J. E. Kreutz, A. Fok, and R. F. Ismagilov, Lab Chip **10**, 2666 (2010).
[6] Z. Chen, P. Liao, F. Zhang, M. Jiang, Y. Zhu, and Y. Huang, Lab Chip **17**, 235 (2017).
[7] F. Schuler, F. Schwemmer, M. Trotter, S. Wadle, R. Zengerle, F. von Stetten, and N. Paust, Lab Chip **15**, 2759 (2015).
[8] A. D. Tadmor, E. A. Ottesen, J. R. Leadbetter, and R. Phillips, Science **333**, 58 (2011).
[9] B. Vogelstein and K. W. Kinzler, Proc. Natl. Acad. Sci. U.S.A **96**, 9236 (1999).
[10] X. Bian, F. Jing, G. Li, X. Fan, C. Jia, H. Zhou, Q. Jin, and J. Zhao, Biosens. Bioelectron. **74**, 770 (2015).
[11] E. Day, P. H. Dear, and F. McCaughan, Methods **59**, 101 (2013).
[12] P. Wang, F. Jing, G. Li, Z. Wu, Z. Cheng, J. Zhang, H. Zhang, C. Jia, Q. Jin, and H. Mao, Biosens. Bioelectron. **74**, 836 (2015).
[13] Y. D. Lo, F. M. Lun, K. A. Chan, N. B. Tsui, K. C. Chong, T. K. Lau, T. Y. Leung, B. C. Zee, C. R. Cantor, and R. W. Chiu, Proc. Natl. Acad. Sci. U.S.A **104**, 13116 (2007).
[14] Q. Xu, M. Hashimoto, T. T. Dang, T. Hoare, D. S. Kohane, G. M. Whitesides, R. Langer, and D. G. Anderson, Small **5**, 1575 (2009).
[15] L. Y. Chu, A. S. Utada, R. K. Shah, J. W. Kim, and D. A. Weitz, Angew. Chem., Int. Ed. **46**, 8970 (2007).
[16] B. N. Estevinho, F. Rocha, L. Santos, and A. Alves, Trends Food Sci. Technol. **31**, 138 (2013).
[17] J. Renukuntla, A. D. Vadlapudi, A. Patel, S. H. Boddu, and A. K. Mitra, Int. J. Pharm. **447**, 75 (2013).
[18] A. Ammala, Int. J. Cosmetic Sci. **35**, 113 (2013).
[19] A. Abbaspourrad, N. J. Carroll, S. H. Kim, and D. A. Weitz, Adv. Mater. **25**, 3215 (2013).
[20] C. N. Baroud, F. Gallaire, and R. Dangla, Lab Chip **10**, 2032 (2010).
[21] P. Zhu and L. Wang, Lab Chip **17**, 34 (2017).
[22] J. Nunes, S. Tsai, J. Wan, and H. Stone, J. Phys. D: Appl. Phys. **46**, 114002 (2013).
[23] E. Amstad, M. Chemama, M. Eggersdorfer, L. Arriaga, M. Brenner, and D. Weitz, Lab Chip **16**, 4163 (2016).

[24]A. J. Teo, K.-H. H. Li, N.-T. Nguyen, W. Guo, N. Heere, H.-D. Xi, C.-W. Tsao, W. Li, and S. H. Tan, Anal. Chem. **89**, 4387 (2017).

[25]K. C. van Dijke, K. C. Schroën, and R. M. Boom, Langmuir **24**, 10107 (2008).

[26]G. Vladisavljević, I. Kobayashi, and M. Nakajima, Microfluid. Nanofluid. **13**, 151 (2012).

[27]I. Kobayashi, S. Mukataka, and M. Nakajima, Ind. Eng. Chem. Res. **44**, 5852 (2005).

[28]I. Kobayashi, S. Mukataka, and M. Nakajima, J. Colloid Interface Sci. **279**, 277 (2004).

[29]I. Kobayashi, S. Mukataka, and M. Nakajima, Langmuir **21**, 7629 (2005).

[30]K. van Dijke, G. Veldhuis, K. Schroën, and R. Boom, Lab Chip **9**, 2824 (2009).

[31]R. Dangla, S. C. Kayi, and C. N. Baroud, Proc. Natl. Acad. Sci. U.S.A **110**, 853 (2013).

[32]I. Kobayashi, Y. Wada, K. Uemura, and M. Nakajima, Microfluid. Nanofluid. **8**, 255 (2010).

[33]G. T. Vladisavljević, E. E. Ekanem, Z. Zhang, N. Khalid, I. Kobayashi, and M. Nakajima, Chem. Eng. J. **333**, 380 (2018).

[34]A. Ofner, D. G. Moore, P. A. Rühs, P. Schwendimann, M. Eggersdorfer, E. Amstad, D. A. Weitz, and A. R. Studart, Macromol. Chem. Phys. **218**, 1600472 (2017).

[35]M. B. Esch, S. Kapur, G. Irizarry, and V. Genova, Lab Chip **3**, 121 (2003).

[36]M. Leester-Schädel, T. Lorenz, F. Jürgens, and C. Richter, (Springer International Publishing, 2016), Vol. 23.

[37]J. Zhou, D. A. Khodakov, A. V. Ellis, and N. H. Voelcker, Electrophoresis **33**, 89 (2012).

[38]S. H. Tan, N.-T. Nguyen, Y. C. Chua, and T. G. Kang, Biomicrofluidics **4**, 032204 (2010).

[39]R. Williams, S. G. Peisajovich, O. J. Miller, S. Magdassi, D. S. Tawfik, and A. D. Griffiths, Nat. Methods **3**, 545 (2006).

[40]A. C. Hatch, J. S. Fisher, S. L. Pentoney, D. L. Yang, and A. P. Lee, Lab Chip **11**, 2509 (2011).

[41]J.-C. Baret, Lab Chip **12**, 422 (2012).

[42]T. C. Lorenz, J. Visualized Exp. **63**, e3998 (2012).

[43]A. C. Hatch, J. S. Fisher, A. R. Tovar, A. T. Hsieh, R. Lin, S. L. Pentoney, D. L. Yang, and A. P. Lee, Lab Chip **11**, 3838 (2011).

[44]Y. Men, Y. Fu, Z. Chen, P. A. Sims, W. J. Greenleaf, and Y. Huang, Anal. Chem. **84**, 4262 (2012).

[45]Q. Zhu, Y. Gao, B. Yu, H. Ren, L. Qiu, S. Han, W. Jin, Q. Jin, and Y. Mu, Lab Chip **12**, 4755 (2012).

[46]Q. Zhu, L. Qiu, B. Yu, Y. Xu, Y. Gao, T. Pan, Q. Tian, Q. Song, W. Jin, and Q. Jin, Lab Chip **14**, 1176 (2014).

[47]N. Mittal, C. Cohen, J. Bibette, and N. Bremond, Phys. Fluids **26**, 082109 (2014).

[48]R. Dangla, E. Fradet, Y. Lopez, and C. N. Baroud, J. Phys. D: Appl. Phys. **46**, 114003 (2013).

[49]Z. Li, A. Leshansky, L. Pismen, and P. Tabeling, Lab Chip **15**, 1023 (2015).

[50]M. Stoffel, S. Wahl, E. Lorenceau, R. Höhler, B. Mercier, and D. E. Angelescu, Phys. Rev. Lett. **108**, 198302 (2012).

[51]C. Priest, S. Herminghaus, and R. Seemann, Appl. Phys. Lett. **88**, 024106 (2006).

[52]T. Nisisako and T. Torii, Lab Chip **8**, 287 (2008).

[53]M. B. Romanowsky, A. R. Abate, A. Rotem, C. Holtze, and D. A. Weitz, Lab Chip **12**, 802 (2012).

[54]M. Muluneh and D. Issadore, Lab Chip **13**, 4750 (2013).

[55]H.-H. Jeong, V. R. Yelleswarapu, S. Yadavali, D. Issadore, and D. Lee, Lab Chip **15**, 4387 (2015).

[56]R. Seemann, M. Brinkmann, T. Pfohl, and S. Herminghaus, Rep. Prog. Phys. **75**, 016601 (2012).

[57]B. J. Hindson, K. D. Ness, D. A. Masquelier, P. Belgrader, N. J. Heredia, A. J. Makarewicz, I. J. Bright, M. Y. Lucero, A. L. Hiddessen, and T. C. Legler, Anal. Chem. **83**, 8604 (2011).

[58]D. Pekin, Y. Skhiri, J.-C. Baret, D. Le Corre, L. Mazutis, C. B. Salem, F. Millot, A. El Harrak, J. B. Hutchison, and J. W. Larson, Lab Chip **11**, 2156 (2011).